Research Report

Electrical Testing of Gold Nanostructures by Conducting Atomic Force Microscopy

Alexander Bietsch[1], M. Alexander Schneider[2], Mark E. Welland[2], and Bruno Michel[1]

[1]IBM Research
Zurich Research Laboratory
8803 Rüschlikon
Switzerland

[2]University of Cambridge
Dept. of Engineering
Cambridge CB2 1PZ
UK

IBM Research
Almaden · Austin · Beijing · Haifa · T.J. Watson · Tokyo · Zurich

Electrical Testing of Gold Nanostructures by Conducting Atomic Force Microscopy

Alexander Bietsch[1], M. Alexander Schneider[2], Mark E. Welland[2], and Bruno Michel[1]

[1]*IBM Research, Zurich Research Laboratory, 8803 Rüschlikon, Switzerland*
[2]*University of Cambridge, Dept. of Engineering, Trumpington Street, Cambridge CB2 1PZ, UK*

Abstract

We devised a method for the reliable electrical testing of nanoscale wire arrays using conducting probe atomic force microscopy (AFM) in ambient conditions. A key requirement of this approach is the formation of highly reproducible electrical contacts between the conductive tip and the sample. We discuss the basic mechanical and electrical criteria of nanocontacts and derive a force-controlled protocol for the formation of low-Ohmic contacts. Tips sputter-coated with platinum provided the mechanical stability for both tapping-mode imaging and the formation of low-Ohmic contacts on gold samples. Nanostructures on the sample were identified by topographic imaging and subsequently probed using the AFM tip as a mobile electrode. We measured resistivities in arrays of nanowires or local potentials of wires within electrical circuits, and detected electrical failures, thermal gradients, and small geometrical variations. The ability of this instrument to address electrical characteristics with high spatial resolution makes it a powerful tool for lithography developments and on-chip monitoring of nanoscale circuits.

I. INTRODUCTION

With the characteristic dimensions of microelectronic circuits approaching the nanoscale, new tools are needed to test and characterize their elements. In semiconductor manufacturing, electrical probing is done on specialized test structures only that are equipped with micronsized contact pads. Clever application of electrical metrology can yield useful data concerning linewidth variations, defects, or overlay accuracy of lithography processes. Probing on actual devices is not possible because the circuits would be damaged by a macroscopic probe tip. Scanning electron microscopy (SEM) is useful for visual inspection and noninvasive testing of electrical insulation ($>10^{11}\,\Omega$) of microelectronic structures [1], but it cannot determine conductivity and topographic profiles accurately on intact chips. Scanning probe microscopes image surfaces in a nondestructive manner by scanning a sharp tip over the surface with subnanometer precision using piezoelectric actuators. Scanning tunneling microscopy can test topographical and electronic properties only on fully conductive surfaces, whereas atomic force microscopy (AFM) [2] provides topographic images of arbitrary samples having conductive or insulating regions. Electrical information on the sample can be obtained with conductive AFM tips. Standard AFM probes microfabricated of Si or SiN are poorly conductive even when they are highly doped. Coatings of metals or boron-doped diamond [3] provide improved conductivity. Noncontact schemes are preferable for electrical measurements to avoid the destructive mechanical stresses involved with contact-mode scanning: In electrostatic force microscopy [4] or Kelvin probe microscopy [5] the tip oscillates a few nanometers above the surface to sense Coulomb forces or surface potentials with millivolt accuracy and a lateral resolution as good as 100 nm [6]. Another method is scanning capacitance microscopy, where the tip is oscillated in tapping mode and the variation of tip–sample capacitance is related to dopant profiles [7,8] or buried metal structures [9]. In a similar way, applied microwave fields between tip and substrate can be used to detect electronic properties of the substrate [10,11].

The most direct approach for electrical characterization is to use a conductive tip to establish an electrical contact at various positions on the sample. Tips used for this task have to be mechanically robust to survive the forces applied when scanning and the additional forces to form an electrical contact by penetrating or displacing contaminant and passivation layers. These may be present on tip and sample at ambient conditions. Tips should also be chemically inert to avoid passivation by oxidation or electrochemically induced reactions that could interfere with their conductivity. In addition they should be sharp enough to provide a good resolution of scan images. Silicon tips oxidize in air and have high contact resistances [12,13]. High conductivity was reported for coatings of Au, Ag, or Pt with contact resistances on a gold sample down to 30 Ω, but these tips are susceptible to wear [13,14]. Coatings of borondoped diamond provide excellent mechanical stability and promising electrical properties, but contamination of the tip can compromise its conductivity [12,14]. Conductive diamond tips have been used successfully for AFM applications such as high-resolution scanning resistance profiling on the nanoscale [15,16], local electrical characterization of semiconducting films [17] or organic crystals [18], and potential measurements on semiconductor devices [19] or gold nanowires [20]. Gold-coated tips have been used to probe conduction in percolating nanocomposites [21]. Semiconductor quantum dots were studied using tips coated with Pd or a Au:Pd alloy [22]. Pt-coated tips were used to investigate changes in conductivity through Langmuir–Blodgett films [23].

All of the above systems operated on highly resistive samples or with large resistors in series with the tip. The difficulties of forming reproducible tip–sample contacts have so far foiled convincing applications of conducting AFM in the regime below 1 kΩ. This regime must be entered to characterize metallic interconnects of submicron dimensions where the conductivity

can no longer be obtained from bulk parameters. The resistivity typically increases due to enhanced scattering at surfaces or grain boundaries. When the structures are larger than $\sim$10 nm, quantum effects are not evident at room temperature, but the granular structure of a metal film makes a theoretical prediction of conductivity difficult and complex [24,25]. Measurements are needed to determine the effective resistivities.

In this article we demonstrate electrical metrology on gold nanostructures. We discuss the mechanical and electrical properties of metallic tip–sample contacts and introduce tips and protocols for reliable electrical probing using the force and position control of an AFM. The regime we addressed was that of contacts with a radius of $\sim$10 nm, large enough to rule out quantum effects and to achieve good and reliable conductance for accurate conductivity and potential probing, but small enough to provide sufficient spatial resolution to resolve 50-nm-wide wires.

II. THEORY: NANOCONTACTS

Establishing an electrical contact between a probe tip and a metal surface is common in various types of electrical testing. The resistance of a macroscopic constriction in a homogeneous conductor can be described classically by the Maxwell formula

$$R_{\mathrm{Maxwell}} = \frac{\rho}{2a} \, , \tag{1}$$

assuming a symmetrical case with constant resistivity ρ and a radius of the contact area a. This formula is valid for the diffusive limit, when a is large compared to the mean free path of electrons. When contact zones are reduced to a few atoms, electron transport is ballistic and the conductivity is described by the Landauer–Büttiker formalism in terms of the transmission of conductance channels through the junction [26]. The number of conductance channels is proportional to the area of contact in scales of the Fermi wavelength. Transmission coefficients are close to unity when no scattering sites such as impurities or grain boundaries are involved at the constriction. Quantized conductance can be observed for small contacts when only a few channels are involved. When the contact radius a is large compared to the Fermi wavelength λ_{F}, as is the case in our experiments, the resistance converges to the Sharvin formula [27–29]

$$R_{\mathrm{Sharvin}} = \frac{h}{2e^2} \frac{\lambda_{\mathrm{F}}^2}{\pi^2 a^2} \, . \tag{2}$$

This formula holds for a nanoscale constriction of homogeneous material. In a real contact between a tip and a surface of different materials the transmission coefficients may be reduced owing to interface scattering. The material with the greater Fermi wavelength provides fewer conductance channels and thus constitutes the bottleneck of the ballistic transmission.

The contact area between an elastic tip and a flat sample depends on the shape of the tip and the applied load. The mechanics of an elastic contact of a sphere on a surface were modeled first by Hertz [30],

$$a_{\mathrm{Hertz}} = \left(\frac{3Pr}{4E^*} \right)^{\frac{1}{3}} \, , \tag{3}$$

where a_{Hertz} is the radius of contact, P the applied load, r the tip radius, and $E^* = \left[\frac{1-\nu_1}{E_1} + \frac{1-\nu_2}{E_2} \right]^{-1}$ the effective elastic modulus combined from Young's moduli E_1, E_2 and Poisson's numbers ν_1, ν_2 of tip and surface materials, respectively. On a curved substrate, r is replaced by an effective radius

$$r_{\mathrm{eff}} = \frac{r_{\mathrm{tip}} r_{\mathrm{surface}}}{(r_{\mathrm{tip}} + r_{\mathrm{surface}})}, \tag{4}$$

where r_{tip} is the tip radius and r_{surface} is the radius of curvature of the substrate surface. When the contact area is smaller than the grain size of the substrate, the surface roughness should be taken into account by the local radius of curvature of the grains.

More detailed models also take adhesive interactions into account, which is particularly important for small geometries and moderate loads. The approximation suggested by Derjaguin, Muller and Toporov (DMT) [31] adds the adhesive force to the applied load of the Hertzian model

$$a_{\mathrm{DMT}} = \left(\frac{3(P + 2\pi w r)r}{4E^*} \right)^{\frac{1}{3}}, \tag{5}$$

where w is the work of adhesion. A model introduced by Johnson et al. (JKR model) [32] considers specific stress and deformations due to adhesive forces inside the contact zone that further increase the radius of contact. More refined theories were introduced by Maugis [33], and Greenwood and Johnson [34]. Experiments carried out with AFM tips in ultrahigh vacuum agreed well with the model by Maugis [35,36]. But at ambient conditions, contaminants on surfaces like gold tend to reduce adhesive interactions at the perimeter of the contact zone. In the limit, monolayers of alkanethiols on gold can reduce the adhesion so far that the Hertz model is the best fit [37]. For our experiments in ambient conditions we favored the DMT model, because the effect of adhesion is lower than that of the Maugis and JKR models, and it provides simple analytical expressions for our calculations.

Even at low loads, contact pressures of small spherical tips can exceed the yield strength Y of the materials involved. Following Ref. [38], the maximum contact pressure p_0 can be expressed by a ratio of the contact radius a to the tip radius:

$$p_0 = \frac{2E^* a}{\pi r} \tag{6}$$

The onset of plastic yield occurs at $p_0 = 1.6\, Y$. Assuming typical bulk values for the material constants and using the DMT expression, Eq. (5), for the contact radius, electrical probing on a metal with a submicron-sized tip would always cause plastic deformations. At the nanoscale, however, the generation and motion of dislocations require relatively higher stresses. This effect improves the yield strength of small structures or nanocrystalline materials by more than one order of magnitude compared to bulk materials. For metals with grain sizes down to $d \approx 10$ nm, hardness typically follows the Hall–Petch relation and increases proportional to $\sim d^{-1/2}$ [39]. Consequently, nano-indentation experiments on metal surfaces [40] and nanoscale contact experiments with metal tips on gold surfaces show increased yield strengths for both tips and surfaces [41–44].

III. EXPERIMENTAL

A. Instrumentation

In the conducting AFM setup we used a commercial scan head featuring optical detection of the deflection of the cantilever (Dimension 3000, Digital Instruments, CA). Electrical contact to the probe tip was established by the metal clamp of a standard tip holder. The only modifications to the tip holders were a wire providing ground connection to the (I–V)

converter and a 10-Ω resistor used to divide the voltage for conductivity probing. The scan head was mounted on a motorized translation stage for vertical positioning. The sample was scanned using an x-y scan stage with capacitive feedback (P731.20, Physik Instrumente, Germany) allowing hysteresis–free absolute positioning with nanometer accuracy. This scanner was mounted on motorized translation stages for lateral coarse displacement of the sample. The entire setup was protected by an aluminum box and placed on a vibration isolation table. The system was connected to a control system based on a digital signal processor (DSP), an analog interface (East Coast Scientific, UK), and a software that allowed the flexible control of scanning probe experiments (Topo, IBM Zurich Research Laboratory, Switzerland). Output voltages of the analog interface and the frequency generator were divided by resistors to appropriate values before being applied to tip or sample. Currents were measured using home-built I–V converters.

B. Electrical Probing

For conductivity probing experiments, Fig. 1a, the AFM tip acted as a mobile electrode to apply the input voltage (V) to the nanowire sample. An I–V converter connected to the sample measured the current. The I–V converter had an amplification factor of 10^7 V/A, a bandwidth of 200 Hz, and a noise level of 4 nA$_{\text{rms}}$.
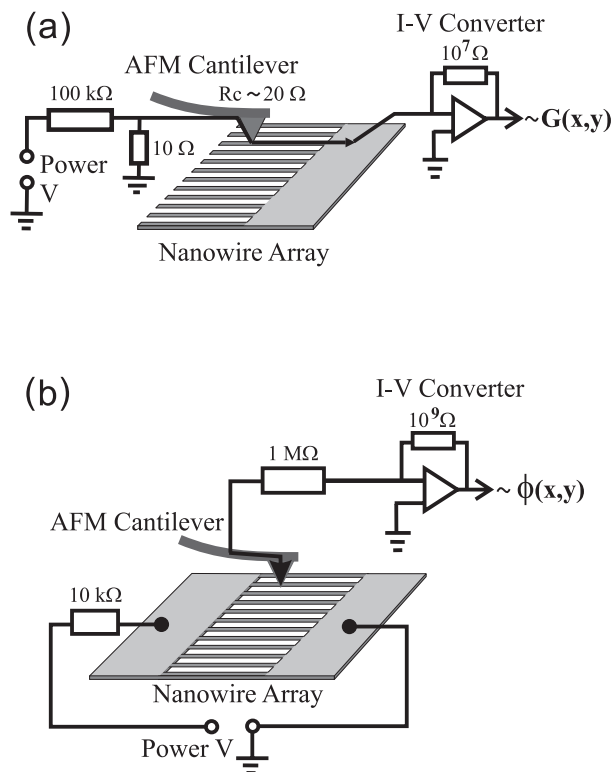

FIG. 1. Measurement schemes for testing nanowires with a conducting AFM cantilever as a mobile probe electrode: (a) Conductivity probing: Comb-like wire array with a common electrode and the AFM tip as the second electrode. The current I measured by this two-point probing is proportional to the lateral conductivity $G(x, y)$ between tip and sample electrode. (b) Potential probing: Array of wires in a closed electrical circuit. A small amount of current I that is proportional to the local potential $\phi(x, y)$ is picked up by the AFM tip, which thus acts as a potential probe.

In potential probing measurements, Fig. 1b, an array of nanowires was connected to a voltage source by a 10-kΩ series resistor. The local potential on the nanowires was probed with the AFM tip connected to ground via a 1-MΩ resistor and an I–V converter with a conversion ratio of 10^9 V/A, a bandwidth of 10 kHz, and an rms noise of 15 pA for 1 kHz bandwidth. A lock-in technique was used to remove offset voltages and currents.

Prior to electrical probing, a topographic image of the sample region of interest was recorded operating the AFM in tapping mode (oscillation amplitude <50 nm_{pk-pk}), thus avoiding lateral forces between tip and substrate [13]. The intermittent contact between tip and substrate, however, was too short to acquire the electrical information simultaneously. Electrical experiments were carried out on individual spots of the sample or as a sequence of data points along a line defined using the topographic image as a map. The tip–sample distance was controlled by the feedback loop in tapping mode before and after individual I–V measurements. To form an electrical contact, the tip holder was displaced toward the sample by a defined distance (∼40 nm), and the contact force was determined from the deflection of the cantilever. The motion of the oscillation excitation piezo (typically <0.5 nm_{pk-pk} having a Q factor of >100) did not disturb the measurement. A suitable probing force (∼500 nN) was identified prior to recording electrical data by I–V measurements or potential probing.

C. Test Surfaces

The gold film sample was made by evaporating 1 nm of Ti (99.99%, Johnson Mattey) and 300 nm of Au 99.999%, Goodfellow) onto a silicon wafer using an Edwards FL400 electron-beam (e-beam) evaporator operating at a base pressure of 10^{-7} mbar at an evaporation rate of 0.25 nm s^{-1}. The gold surface had an rms roughness of 1.8 nm, determined by AFM measurements with sharp tips. The grains had a diameter of about 50 nm, and the local radius of curvature varied between 100 and 300 nm. Prior to experiments the sample was sonicated in ethanol (puriss. p.a., Fluka) for 3 min and dried under a stream of nitrogen. The resistance of the gold film including all leads between the sample and the I–V converter was below 1 Ω.

D. Nanowire Samples

Nanowire samples were made by two lithographic layers on silicon chips coated with 80 nm of silicon oxide. Large-scale contact pads and interconnects were created by optical lithography and lift-off of 1 nm of Ti and 50 nm of Au. The high-resolution nanowire patterns were added by e-beam lithography. Therefore, a standard polymethylmethacrylate (PMMA) resist layer of ∼130 nm was spin-coated on the sample and annealed at 150°C. Nanowire patterns were written on the chips using a JEOL JEM4000EX transmission electron microscope modified for e-beam lithography with associated scanning attachments [45]. The samples were developed in a methyl-isobutyl-ketone:isopropanol solution and then rinsed in isopropanol. 1 nm of Cr and 20 nm of Au were evaporated at room temperature at 5×10^{-7} mbar base pressure. The resist was lifted off in acetone. The experiments shown in this report were carried out on a single chip with the nanowires fabricated with the same design.

The width of the wires was measured by AFM using tips classified with a radius of 2 to 5 nm (SuperSharpSilicon^{TM} tips, Nanosensors, Germany). The cross sections of the wires were not rectangular but rounded with a radius equal to the wire thickness. The bottom width (reduced by the estimated tip diameter) was 67 ± 5 nm, the width at half the height (FWHM) was 49 ± 5 nm, and the errors are standard deviations including both variations of the sample

and the uncertainty of the tip radius. We calculated a wire cross-section area of 1.2×10^{-15} m^2, using a half circle with the radius corresponding to the gold thickness for the two edges plus a 27-nm-wide rectangular central part. Using the SEM we measured a width of 51 ± 5 nm, which corresponds to the FWHM value. Inspection of the sample by SEM caused an insulating layer to develop on the surface, which interfered with probing experiments. Oxygen-plasma treatment partially removed this layer so that the conducting AFM tip could penetrate it.

E. Platinum-coated Tips

Commercially available silicon cantilevers (Pointprobe, Nanosensors, Germany) with force constants of $\sim$40 N/m and resonance frequencies of $\sim$300 kHz were dc sputter-coated using a Magnetron Sputter Instrument (LA440, von Ardenne, Germany) in 12 μbar of argon at a distance of 5 cm between target and substrate. First, 10 nm Ti was deposited at a power of 200 W, immediately followed by 180 nm Pt (99.9%, SenVac, Germany) sputtered at 100 W at a rate of 0.75 nm/s. The resistance of the deposited metal film was 0.8 $\Omega/\square$, which led to a resistance of the platinum film 4–5 Ω between the clamp contact of the cantilever holder and the tip.

Inspection of tips by SEM prior to conducting AFM experiments was not possible because of a deposited contamination layer. Several tips were sputtered in a batch and some of them were characterized by SEM, see Fig. 2a. The coating enlarged the tip radius from initially $\sim$10 nm to 50–70 nm. The layer deposited on the backside of the cantilever had a thickness of $\sim$70 nm.

The force constant k of platinum-coated cantilever beams was calibrated using the formula $k = m^*\omega^2$. The effective mass $m^* = 0.24(m_{\mathrm{beam}} + m_{\mathrm{coating}}) + m_{\mathrm{tip}}$ was calculated from the geometric dimensions of lever and coating, and the resonance frequency ω was measured in the AFM setup. The platinum coating increased the force constant by about 25%. The error in determining the force constant was estimated to be of the order of 25%.

Sputtered platinum coatings were mechanically stable for tapping-mode imaging and wire testing as opposed to e-beam evaporated films of Pt or Au of similar thickness, also including an adhesion layer of Ti. The evaporations were carried out at a base pressure of 10^{-7} mbar with evaporation rates between 0.1 and 0.5 nm/s.

IV. RESULTS AND DISCUSSION

Initial attempts to acquire both topographic and current information on partially conductive surfaces using contact-mode scans caused rapid wear of conductive coatings on tips. It was impossible to maintain an electrical contact during the lateral displacement in a high-resolution AFM scan when metallized tips were used. Diamond-coated tips (Nanosensors, Germany) could withstand the scanning forces in the regime necessary for electrical contact but did not form a reproducible low-Ohmic contact on polycrystalline gold surfaces: The contact resistance of these tips on gold samples was of the order of 10 kΩ and varied by about $\pm$50%. We attributed these instabilities to nanoscale geometric variations in the contact zone between the diamond grain and the gold surface induced by the topography of the sample. Alternatively, we tested metal-coated silicon tips in both tapping-mode imaging and electrical probing. Evaporated coatings of Au or Pt (including Ti as an adhesion layer) were damaged within a few probing approaches. Tips *sputter-coated* with platinum, however, (Fig. 2) had sufficiently long lifetimes for our experiments. Locations of interest were identified in a topo-
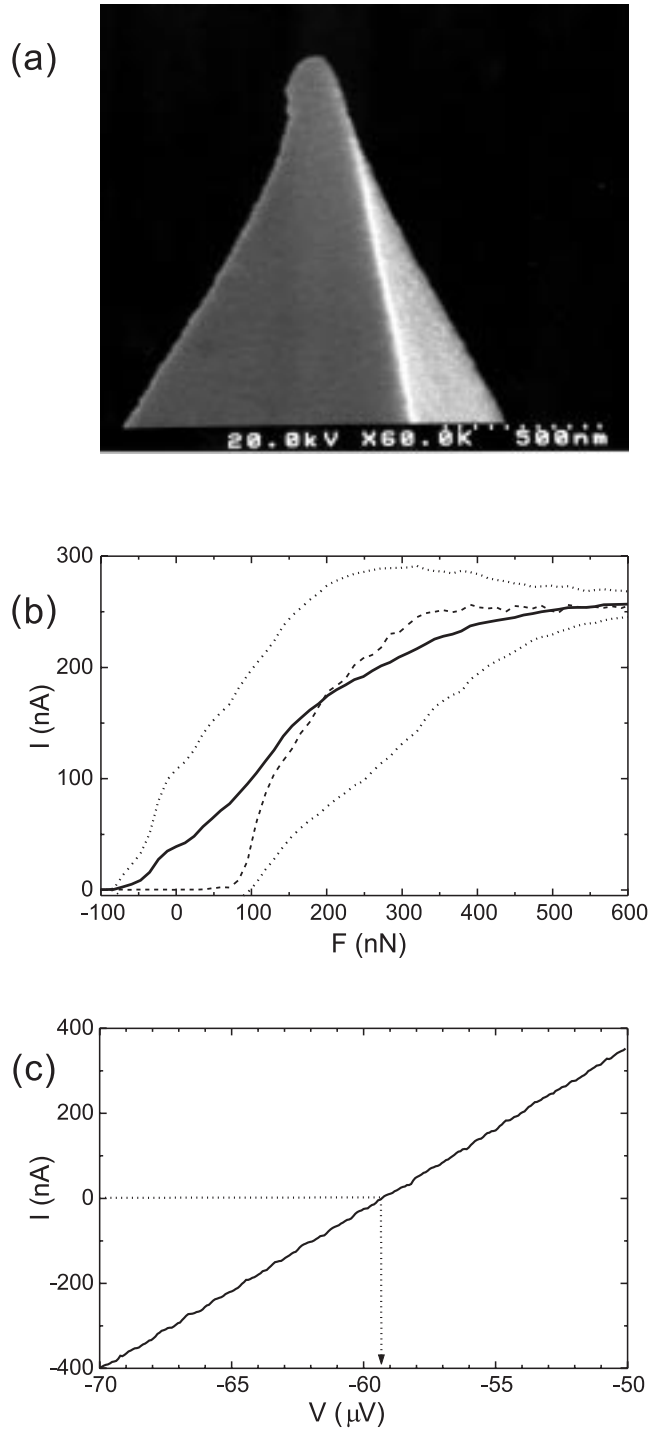
FIG. 2. Tip characterization. (a) Scanning electron microscope image of an AFM tip sputter-coated with platinum; the tip radius is ~70 nm. (b) Average of 16 current vs. force experiments (bold line) using a platinum tip on a gold sample with a voltage of -50 μV applied to the tip. The standard deviation of the measurements is indicated by dotted lines. The dashed line shows a single nonaveraged experiment. (c) Current vs. voltage plot at a force of 600 nN resulting in a total resistance of $R = 26$ Ω.

graphic tapping-mode scan to perform selective tip approaches to a series of spots where we took electrical measurements.

A. Reversible Formation of Electrical Contacts

The formation of electrical contact between a gold sample and platinum-coated tips was characterized by recording the current in a series of tip–sample approaches at various positions of the sample. The results are given in the current–force plots of Fig. 2b. The dashed line shows the current during a single non-averaged approach. A steep increase of conductivity was observed above a threshold force of 80 nN, which then leveled off above 300 nN. The threshold force for the onset of conduction was variable (between -80 nN and $+100$ nN), whereas the current at higher forces was more reproducible. For low forces, the resulting average curve (solid line) showed an increasing current with large standard deviation (dotted lines) caused mainly by the variable onset of conduction. This variation reflects the instability during tip–sample approach when the tip snaps into contact with the sample, in addition to variations induced by the local topography and a non-uniform layer of contaminants. At higher forces the current adopted a reproducible behavior as seen from the narrowing bandwidth of the standard deviation curves. In this regime the current increased only slowly with increasing force. The behavior here is consistent with the mechanical and electrical models for a nanocontact, but the reproducible part of the curve is too short to confirm the models. Figure 2b indicated that forces of between 500 and 600 nN were suitable for the formation of good electrical contacts. At these contact forces, I–V measurements showed a linear behavior reflecting the Ohmic characteristic of a metallic contact with a slope corresponding to 27 Ω (Fig. 2c). Resistances at different positions on the sample were reproducible to within a standard deviation of 1 Ω. After subtracting the resistance inherent to the setup we obtained a resistance of the tip-sample contact of $R_{\text{contact}} \approx 11$ Ω. This value was compared with the tip–sample resistance expected from theory.

The following parameters were used: Elastic constants for gold (Young's modulus $E_{\text{Au}} = 78$ GPa, Poisson number $\nu_{\text{Au}} = 0.42$) and platinum ($E_{\text{Pt}} = 170$ GPa, $\nu_{Pt} = 0.39$), work of adhesion between platinum and gold of $w = 4$ Jm^{-2} [46], radius of the tip (70 nm), and the surface roughness ($r_{\text{substrate}} = 200 \pm 100$ nm). For a force of 600 nN we calculated the radius of the contact area to be $a_{\text{DMT}} = 10$ nm. The contact radius determines the limit of spatial resolution. For the Maxwell formula we used the arithmetic mean of the specific resistivities of gold and platinum ($\rho_{\text{Au}} = 2.2$ $\mu\Omega$ cm and $\rho_{\text{Pt}} = 10.7$ $\mu\Omega$ cm) and obtained a contact resistance of 3.1 Ω. Platinum has a larger Fermi wavelength ($\lambda_{F,\text{Pt}} = 0.59$ nm) than gold and thus dominates the ballistic resistance, Eq. (2), of 4.1 Ω. For contacts of 10 nm radius both the ballistic point of view and the diffusive aspect of electronic transport are relevant, so we assume that the combination of both models should lead to a resistance in between the single values given by the models and their sum of $\sim$7 Ω. The measured contact resistance (11 Ω) is of the same order of magnitude. The discrepancy is not surprising for several reasons: One cannot expect a perfect transmission of the conduction channels as assumed in the Sharvin formula because additional scattering at the interface of the contact between gold and platinum may increase the resistance. We used bulk values for the resistivities in the Maxwell formula although the resistivities are typically higher in thin metal films. Furthermore, we have no direct control over the radius of contact and, in that context also, the effect of surface contaminants is difficult to evaluate. We suggest that contaminants are driven out of the contact zone, but they may lower the work of adhesion at the perimeter of the contact zone and thus reduce the radius of contact.

At forces up to $\sim$600 nN we did not observe changes on AFM scans recorded before and after the electrical experiments, indicating that neither tip nor sample have suffered noticeable plastic deformations. At higher forces of $\sim$1000 nN we entered the irreversible plastic regime with the tip leaving indentation wells on the gold surface that were identified on subsequent

scans.

To get an idea of the mechanical stability of the tip–sample contact we calculated the maximum contact pressure p_0 (right-hand scale of Fig. 3a) or the corresponding critical yield stress (left-hand scale) depending on the tip radius (bottom axis). Irreversible plastic deformation occurs when the materials involved are weaker than the indicated critical yield strength. The calculations are based on Eqs. (4)–(6), using the elastic parameters and work of adhesion for Pt and Au (see above). The solid line indicates the yield strength required for a platinum tip on a flat surface without external forces applied, considering adhesion forces only. The plot monitors the increasing stress on sharper tips. A rough sample surface with grains equivalent to a radius of curvature of $r_{\mathrm{surface}} = 200$ nm requires even stronger materials (dashed line). The dotted horizontal line indicates the pressure of 8.2 GPa corresponding to the above experiments leading to a good electrical contact. This pressure was sufficiently high for the tip to penetrate the contamination layer and to establish a metallic contact. The absence of plastic deformations in the experiments suggests a yield strength of at least 5.2 GPa, which is one order of magnitude higher than the bulk values of platinum ($Y_{\mathrm{Pt}} = 0.30$ GPa) and gold ($Y_{\mathrm{Au}} = 0.27$ GPa). The observed stability clearly demonstrates the phenomenon of material hardening at the nanoscale [39–44], and partially compensates for the increased demands of small tip radii. Plastic deformations observed for higher pressures ($p_0 \approx 8.8$ GPa) indicated that we were operating close to the yield strength of the materials involved.

The dashed line in Fig. 3b shows the radius of the contact zone a (right-hand scale) as a function of the tip radius at a pressure of $p_0 = 8.2$ GPa, taking into account an average surface roughness ($r_{\mathrm{surface}} = 200$ nm). For small tips (<43 nm, dotted vertical line) the adhesion forces cause higher contact pressures than our reference of 8.2 GPa, hence this pressure is no longer relevant. In this case we considered it more realistic to keep the externally applied load at zero than to reduce the pressure by retracting forces. Consequently, we extrapolated the curves to the left, assuming zero applied load. The diameter of the contact zone corresponds to the lateral resolution in a probing experiment. Smaller objects increase the contact resistance because of the reduced contact zone.

The size of the contact zone varies with the local surface curvature on a rough surface, Eqs. (4) and (5). In the following we considered the sum of Sharvin and Maxwell resistance as the contact resistance. For our model surface with r_{surface} ranging from 100 to 300 nm we calculated the corresponding variation of contact resistance ΔR. This variation decreases with increasing tip radius as shown by the solid curve in Fig. 3b (left-hand scale). We see in the figure that a higher reproducibility of contact resistance is achieved with larger tips. The calculations confirmed that the radius of our platinum-coated tips (70 nm) was a good compromise to achieve good electrical accuracy for resistance measurements ($\Delta R = 2.2\ \Omega$) and sufficient spatial resolution ($2a = 21$ nm).

With the platinum tips on gold we observed an offset voltage of between 30 and 70 μV. We attributed this voltage to a thermoelectric effect (Seebeck effect) caused by a heating of the cantilever by the laser spot present in typical AFM setups that use optical detection of cantilever deflection. The level of the effect varied with different positions of the manually adjusted laser spot on the cantilever. The value of the thermoelectric force was determined from I–V measurements, where the applied bias balanced the contact potential at zero current. We verified the origin of the offset voltage using diamond-coated tips where the laser-induced potential was much more pronounced with $\sim$500 mV. When the laser was switched off, the contact voltage vanished. Assuming bulk values for the thermoelectric power between Au and Pt of $\sim$1.4 μV/°C at 40°C (interpolated value from [47]), a voltage of 50 μV reflects a temperature difference of ≈ 36°C between the laser-heated tip–sample contact and the cold contact of the cantilever chip. The thermocouple formed by the tip and a conducting
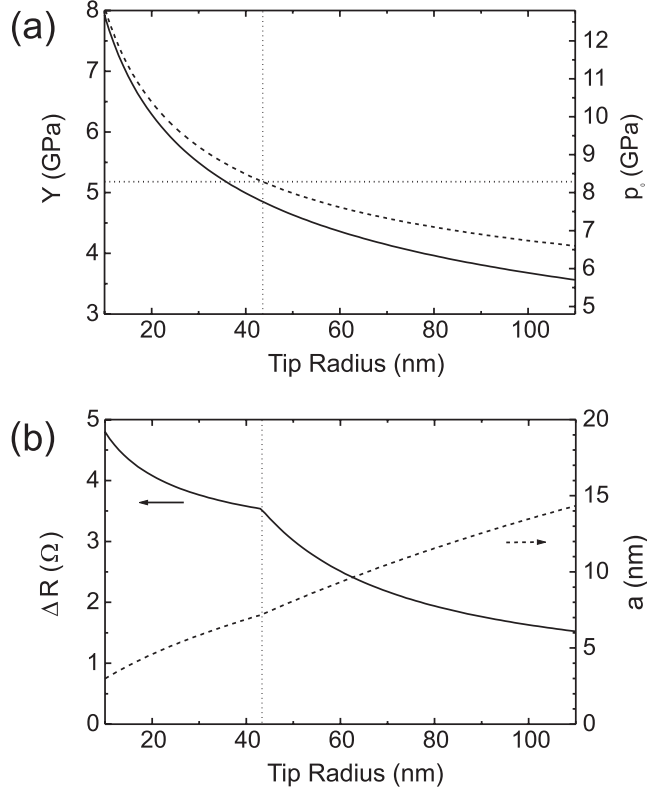
FIG. 3. (a) Minimum yield strength Y (left-hand scale) and the corresponding maximum contact pressure p_0 (right-hand scale) acting between a platinum tip and a gold surface as a function of tip radius. The solid line shows the pressure and critical yield stress calculated for zero applied load (only adhesive forces) on a perfectly flat surface. The stress at zero load increases when surface roughness (mean curvature 200 nm) is also considered (dashed line). The dotted horizontal line indicates a pressure of 8.2 GPa, corresponding to our experimental conditions of electrical contact formation. For tips with a radius smaller than 43 nm the stress due to adhesion forces exceeds this reference value. (b) The roughness-induced variation of contact resistance ΔR (solid line, left-hand scale) on a gold film with the grains having a curvature of 200 ± 100 nm, and the average radius of the contact zone a (dotted curve, right-hand scale) are shown as a function of the tip radius. For large tips the applied load corresponds to a maximum contact pressure of 8.2 GPa. For tips with radii smaller than 43 nm (to the left of the dotted vertical line) the curve was calculated with zero externally applied load.

surface may be useful to probe local variations in heat conductivity and capacity or to analyze temperature distributions to detect hot spots.

B. Characterization of High-Density Nanowire Arrays

1. Conductivity Probing

The conductivity of gold nanowires was tested corresponding to the scheme in Fig. 1a. Comb-like arrays of wires on silicon oxide were fabricated by e-beam lithography. The topography image (Fig. 4a) obtained by a tapping-mode AFM scan with a platinum-coated tip shows the array of gold nanowires (width × thickness × length = 67 nm × 20 nm × 2.8 μm) fabricated by e-beam lithography. The apparent width of the wires in the AFM scan

10

was broadened by the dimensions of the probe tip (radius ~70 nm). Every second wire is intentionally decoupled from the common pad to detect shorts between wires (arrows denote two of the insulating gaps). Conductivity measurements were carried out along the lines indicated in Fig. 4a; resistances were determined from the slopes of the I–V data. The total resistance consisted of constant contributions of the voltage divider resistor (10 Ω), the tip–sample resistance as discussed in the section above, all interconnect wiring on the sample, and the variable contribution from a wire depending on the position of probing. Figure 4b shows the total resistance measured with a step size of 41 nm along three parallel lines across the wire array. The measurement paths deviated 4° from an orientation perpendicular to the wires; this fact is well reflected in the slope (see dotted line) within each series in the plot. The leftmost path in the topography image (squares) was very close to or partially on the common electrode. The data from the other parallel lines spaced 1 μm (circles) and 2 μm (triangles) from the first path clearly show a higher resistance at the wire positions corresponding to the increased distance from the electrode. On the common electrode (squares at the lower right) we find a constant total resistance of 65 Ω with a standard deviation of 2.6 Ω, which served as a reference to evaluate the net wire resistance. In the wire region small clusters of data points correspond to the 14 electrically contacted wires. In the insulating zones zero conductance was measured, hence the resistance is infinite.

Typically, two to four consecutive points were obtained when the wire was crossed with a step size of 41 nm. Data points corresponding to an edge of a wire sometimes showed increased resistance, indicating an incomplete contact, and were not considered for averaging and resistance determination of the nanowires. From the valid data points we determined wire resistivities. Between the left-hand and the middle sections (squares and circles, see Figs. 4a and b) we found resistances per unit length of 94 ± 4 Ω/μm, whereas between the middle and the right-hand sections (circles and triangles) the resistivities were higher, 103 ± 5 Ω/μm.

The specific resistivity $\rho_n = R_n A/l$ of the gold wires was determined from the measured resistivity R_n for a nanowire of length l and a cross-section area A. With $A = 1.2 \cdot 10^{-15}$m^2 (see Section III D) we obtained $\rho_n = 12$ $\mu\Omega$ cm, a value that is more than five times the bulk resistivity of gold ($\rho_{\mathrm{Au}} = 2.2$ $\mu\Omega$ cm). We suggest that the granular structure and the limited size of the wires are the reasons for the high resistivity compared to bulk material.

Figure 4c shows the results of a conductivity measurement along a single nanowire. The linear increase of resistance determined by second-order polynomial regression was 101 ± 5 Ω/μm. Although subject to a high uncertainty, the nonlinear term 1.8 ± 1.9 Ω/μm^2 shows the same tendency of higher resistance towards the end of the wire as the results presented above. The standard deviation of resistance on the wires (5 Ω) was roughly two times greater than on the pad region (2.6 Ω), probably due to the rougher topography of the wire (see topographic image), or because of the discontinuous resistivity induced by the granular structure of the wire.

The increase of resistivity per unit length along the wires can be caused by small changes in their geometry. A possible origin is the proximity artifact in the e-beam lithography process. Scattered electrons from the densely exposed region of the pad electrode can contribute to the exposure of adjacent parts and cause a broadening of the wires in the vicinity of the pads.

Thermal effects are another possible reason for changes in resistance. Temperature enhances the resistivity by 3.9×10^{-3} K^{-1}. Thus a temperature difference of ~25°C would explain the above variations. Current-induced heating can be ruled out because I–V characteristics at our measurement conditions (currents <500 nA) were strictly linear.

Another source of heat was the laser spot on the cantilever. Actually, the temperature of the contact between the hot tip and the sample depended on the local thermal conductivity and capacity of the substrate. The thermoelectric force, which is directly related to temperature
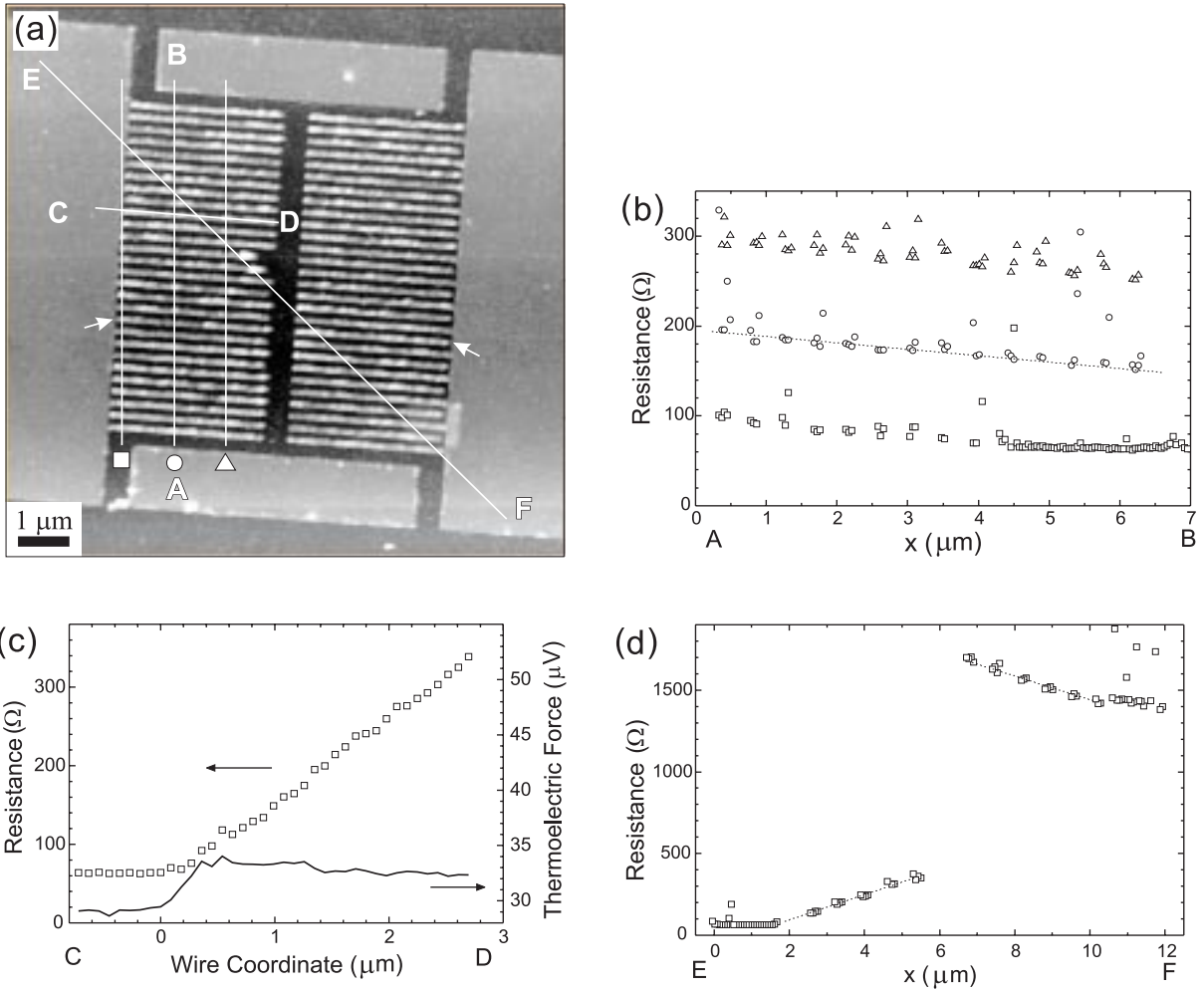
FIG. 4. Conductivity probing. (a) Topographic AFM image of "dual comb" array of gold nanowires (width × thickness × length = 67 nm × 20 nm × 2.8 μm) on silicon oxide (dark in the grayscale). The wires appear to be broadened by a "convolution" with the platinum-coated probe tip (radius 70 nm). Every second wire is intentionally disconnected from the common pad (arrows). Conductivity measurements have been carried out along the sections indicated. (b) Resistance measurements along line A–B in (a). On each conducting wire a cluster of a few data points was obtained. The drop of resistance in each series (dotted line) was caused by the nonperpendicular path across the array. The leftmost path (squares) intersected the pad electrode where the constant resistance served as a reference. (c) The resistance C–D (squares) was constant on the pad electrode and increased with the probed length of a single wire. The thermoelectric force, which is proportional to the temperature of the tip–sample contact (solid line), was also extracted from the I–V data. (d) Probing along a diagonal line E–F across the sample. The resistivities of the wires in the left-hand and right-hand arrays were similar, the absolute slopes of the dotted lines are identical. The significantly higher resistance of ∼1.4 kΩ on the right-hand side of the sample was attributed to an imperfect overlay alignment of the lithographic layers.

differences, was extracted from the I–V data. The thermoelectric force along the wire is shown by the solid line in Fig. 4c. It is constant on the pad electrode (29 μV) and increases to 33 μV within the first 400 nm of the wire. Assuming bulk values for the thermoelectric power (see above), this difference corresponds to a contact temperature on the wire that is about 3°C higher than on the pad electrode, which acts as a heat sink in this context. The decrease

12

by 1.5 μV ($\sim$1°C) along the wire could be explained by an accumulation of heat induced by the measuring sequence, which started at the end of the wire (position B) and moved to the left (position A). The small temperature differences suggest that thermal artifacts have only a minor influence on the measured resistances. We suspect that the increase of resistivity along the wires was thus caused by small geometric variations originating in the lithographic fabrication process.

The data points in Fig. 4d were measured along a line running diagonally across the sample, including pads and wires. This experiment provided an overview of the conductance of the sample region. The wires on both arrays had very similar resistivities, reflected in the same increase of resistance with distance from the corresponding pads. For the pad on the right, however, we observed a constant offset resistance of 1.4 kΩ, which was much higher than the expected resistance of its interconnects in the wiring layout of this pad ($\sim$20 Ω). We attribute this offset to an imperfect overlay of the e-beam-fabricated layer on the optically fabricated interconnects.

2. Potential Measurements

With a potential probing setup (Fig. 1b) we examined an array of nanowires "operated" with an ac voltage of 70 mV$_{rms}$ and a 10-kΩ series resistor. The total resistance of the wire sample was $\sim$280 Ω, including all leads. The total current through the array was 6.8 μA$_{rms}$. Figure 5a shows a topographic AFM scan of the nanowire array in which the gold structures appear as light areas in the grayscale image. The 14 wires had a length of 6.3 μm and a pitch of 400 nm. Two of them were defective and show openings close to the left-hand or right-hand contact pad, circles marked 1 and 2, respectively. The average current through an intact wire was 0.57 μA$_{rms}$. The maximum current picked up by the probe tip was 1.5 nA$_{rms}$.

Figure 5b shows a wire-testing measurement along a line perpendicular to the wires with simultaneous acquisition of topographic information (solid line) and potential information (squares). The height profile did not have the same accuracy as in ordinary scanning because of the additional up-and-down motion for contact formation and because no averaging was implemented for data acquisition of the z position. The large increment between data points (51 nm) and the convolution of the topography with the tip shape allowed only a rough estimate of the wire width. The measurement crossed the wires at about the middle of their length, corresponding to an intermediate potential. Wires with openings marked (1) and (2) were connected to only one of the contact pads and in fact showed the potential of the left-hand (1) or the right-hand (2) pad. The accuracy of the potential measurement does not depend strongly on a good connection between the wires and the tip because of the high Ohmic resistor in series, and is, therefore, less susceptible to poor contacts. Only on the third wire counted from position A did the tip seem to have difficulty establishing contact. There, only one data point with non-zero current was obtained, but the measured current did not fit the potentials mentioned above. This defect was not present in the following measurements so we attributed it to a local contamination.

Along a single wire we followed the potential transition from the left-hand to the right-hand pad, Fig. 5c. The potential was constant on the pads and dropped linearly along the wire. Only at a few points close to the right-hand pad did some data points deviate from this trend, possibly because the surface was contaminated there or the tip missed the wire. The voltage drop from pad to pad (0.35 mV$_{rms}$) corresponds to a wire resistivity of 97 Ω/μm, a value consistent with the results of conductivity probing.

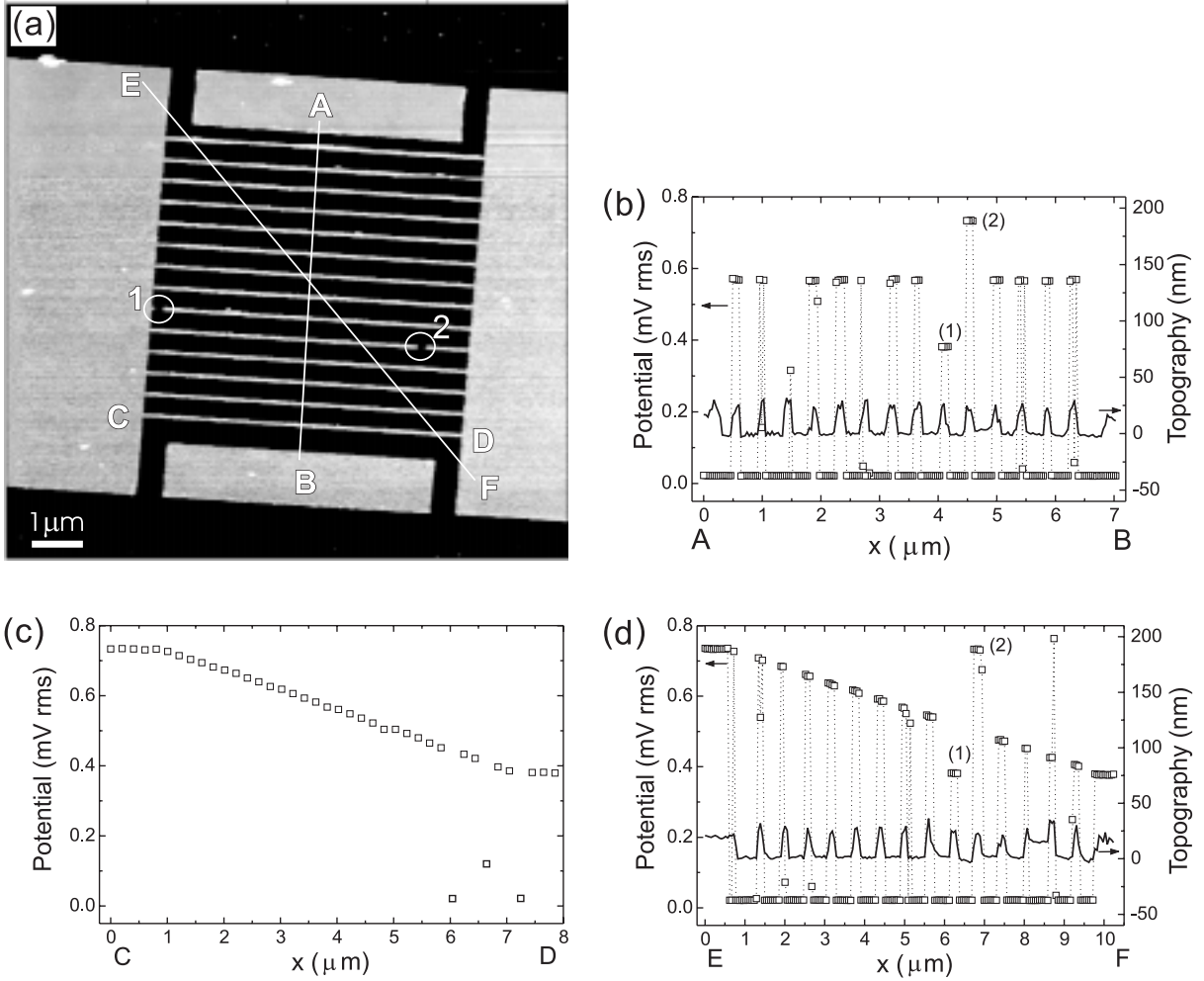A probing scan diagonally across the sample, Fig. 5d, manifests the observations of the

FIG. 5. Potential probing. (a) Topographic AFM scan (using a platinum-coated tip) of a gold wire array on silicon oxide. The apparent width of the wires (width × thickness × length = 67 nm × 20 nm × 6.3 μm) was broadened by the tip radius of 70 nm. Two defects in the wires are marked with circles 1 and 2. (b) The potential (squares) was probed on a path A–B perpendicular to the wires. Intact wires showed an intermediate potential, whereas wires with defects (1) and (2) monitor the potential of the pads to which they were connected. The topography along section A–B was recorded simultaneously (solid line). Probing failed on only one wire. (c) The potential at C–D was constant on the pads and dropped linearly along a single nanowire. (d) Potential (squares) and topography (solid line) on a diagonal scan E–F across the wire sample.

previous plots. Again, the local potentials (squares) depending on the wire coordinates were measured with high accuracy, and the valid data points correlate well with the topography (solid line) of the array. In this plot one can directly see that the potentials of defective wires, (1) and (2), correspond to the flat potentials on the pads.

V. SUMMARY AND OUTLOOK

Electrical testing with today's chip probers is too harmful to address submicron structures directly and requires special test patterns equipped with micron-sized contact pads. This restricts testing to a small number of structures in locations foreseen on the design level. By using mobile, conductive AFM probes, testing of electrical properties against a common

14

macroscopic electrode such as ground or supply voltage becomes possible anywhere on the circuit. Prior to testing, structures are identified in a topographic AFM image using the same tip, thus allowing alignment with nanometer-level accuracy.

We have addressed the question of optimal tip geometry to achieve reliable electrical and accurate topographical information in dense nanowire arrays. Our experiments and calculations show that using a platinum-coated probe tip with a radius of 70 nm can provide low Ohmic contacts, which allow accurate nondestructive testing of 50-nm features as well as large metal patterns. On a gold surface, the diameter of the contact neck under load is close to 20 nm, resulting in a contact resistance of the order of 10 Ω and a substrate roughness-induced resistance variation of less than 2 Ω. The lateral resolution during noncontact scanning of such a tip is about 5 nm, whereas large aspect ratio features are enlarged by the tip width and the angle of the tip cone.

In summary we demonstrated localized, nondestructive electrical probing on dense arrays of wires $\sim$60 nm wide and a few microns long: We measured the conductivity of wires with an accuracy of a few Ohms and obtained statistical information on wire resistances. Potential probing characterized the voltage drop along wires with an accuracy of a few microvolts. In addition we detected temperature variations via the thermoelectric effect.

Besides the platinum–gold model system, other technologically relevant materials such as copper, aluminum, and silicon will be more difficult to probe, however, because they have an insulating oxide layer that must be penetrated. It is not obvious that platinum-coated tips would be the best choice for such an endeavor. Microfabricated cantilevers with integrated metal tips [48] or tip-coating materials based on Ti or W [49] may be alternatives. For potential probing applications the choice of the tip is less critical because larger variations of contact resistance can be tolerated [16,19,20].

At present, AFM is still too slow for accurate high-speed, electrical, critical dimension (CD) measurements, but arrays of independent conductive probes may allow this restriction to be overcome in the next few years. Routine measurements will allow full automation by programmed sequences. By providing topographic and electric information simultaneously with high accuracy, the conducting AFM will be a powerful diagnostic tool for the research and development of high-resolution lithography and microelectronics.

[1] S. S. Mahant-Shetti, T. J. Aton, R. J. Gale, and M. H. Bennett-Lilley, Appl. Phys. Lett. **56**, 2310 (1990).

[2] G. Binnig, C. F. Quate, and C. Gerber, Phys. Rev. Lett. **56**, 930 (1986).

[3] Ph. Niedermann, N. Blanc, R. Christoph, and J. Burger, J. Vac. Sci. Technol. A **14**, 1233 (1996).

[4] J. E. Stern, B. D. Terris, H. J. Mamin, and D. Rugar, Appl. Phys. Lett. **53**, 2717 (1988).

[5] M. Nonnenmacher, M. P. O'Boyle, and H. K. Wickramasinghe, Appl. Phys. Lett. **58**, 2921 (1991).

[6] H. O. Jacobs, P. Leuchtmann, O. J. Homan, and A. Stemmer, J. Appl. Phys. **84**, 1168 (1998).

[7] W. Denk and D. W. Pohl, Appl. Phys. Lett. **59**, 2171 (1991).

[8] J. S. McMurray and C. C. Williams, J. Vac. Sci. Technol. B **15**, 1011 (1997).

[9] J. J. Kopanski and S. Mayo, Appl. Phys. Lett. **72**, 2469 (1998).

[10] G. P. Kochanski, Phys. Rev. Lett. **62**, 2285 (1989).

[11] J.-P. Bourgoin, M. B. Johnson, and B. Michel, Appl. Phys. Lett. **65**, 2045 (1994).

[12] S. J. O'Shea, R. M. Atta, and M. E. Welland, Rev. Sci. Instrum. **66**, 2508 (1995).

[13] R. E. Thomson and J. Moreland, J. Vac. Sci. Technol. B **13**, 1123 (1995).

[14] M. A. Lantz, S. J. O'Shea, and M. E. Welland, Rev. Sci. Instrum. **69**, 1757 (1998).

[15] J. N. Nxumalo, D. T. Shimizu, and D. J. Thomson, J. Vac. Sci. Technol. B **14**, 386 (1996).

[16] P. De Wolf, T. Clarysse, W. Vandervorst, L. Hellemans, P. Niedermann, and W. Hänni, J. Vac. Sci. Technol. B **16**, 355 (1998).

[17] C. Ballif, M. Regula, F. Levy, F. Burmeister, P. Niedermann, T. Matthes, P. Leiderer, W. Gutmannsbauer, and R. Bucher, J. Vac. Sci. Technol. A **16**, 1239 (1998).

[18] M. J. Loiacono, E. L. Granstrom, and C. D. Frisbie, J. Phys. Chem. B **102**, 1679 (1999).

[19] T. Trenkler, P. De Wolf, and W. Vandervorst, J. Vac. Sci. Technol. B **16**, 367 (1998).

[20] M. C. Hersam, A. C. F. Hoole, S. J. O'Shea, and M. E. Welland, Appl. Phys. Lett. **72**, 915 (1998).

[21] E. Z. Luo, I. H. Wilson, X. Yan, and J.B. Xu, Phys. Rev. B **57**, R15120 (1998).

[22] B. Alperson, S. Cohen, I. Rubinstein, and G. Hodes, Phys. Rev. B **52**, R17017 (1995).

[23] K. Yano, M. Kyogaku, R. Kuroda, Y. Shimada, S. Shido, H. Matsuda, K. Takimoto, O. Albrecht, K. Eguchi, and T. Nakagiri, Appl. Phys. Lett. **68**, 188 (1996).

[24] A. F. Mayadas and M. Shatzkes, Phys. Rev. B **1**, 1382 (1970).

[25] G. Palasantzas, Phys. Rev. B **58**, 9685 (1998).

[26] M. Büttiker, Y. Imry, R. Landauer, and S. Pinhas, Phys. Rev. B **31**, 6207 (1985).

[27] Y. V. Sharvin, JETP **21**, 655 (1965).

[28] M. Brandbyge, M. R. Sorensen, P. Stoltze, K. W. Jacobsen, J. K. Norskov, L. Olesen, E. Laegsgaard, I. Stensgaard, and F. Besenbacher, Phys. Rev. B **52**, 8499 (1995).

[29] The Sharvin resistance can also be expressed in fully classical terms by substituting λ_F with ρ and using the electron mean free path λ: $R_{\text{Sharvin}} = 4\rho\lambda/(3\pi a^2)$.

[30] H. Hertz, J. Reine Angew. Math. **92**, 156 (1882).

[31] B. V. Derjaguin, V. M. Muller, and Y. P. Toporov, J. Coll. Interface Sci. **53**, 314 (1975).

[32] K. L. Johnson, K. Kendall, and A. D. Roberts, Proc. R. Soc. London A **324**, 301 (1971).

[33] D. Maugis, J. Coll. Interface Sci. **150**, 243 (1992).

[34] J. A. Greenwood and K. L. Johnson, J. Phys. D **31**, 3279 (1998).

[35] M. A. Lantz, S. J. O'Shea, M. E. Welland, and K. L. Johnson, Phys. Rev. B **55**, 10776 (1997).

[36] M. A. Lantz, S. J. O'Shea, and M. E. Welland, Phys. Rev. B **56**, 15345 (1997).

[37] R. C. Thomas, J. E. Houston, T. A. Michalske, and R. M. Crooks, Science **259**, 1883 (1993).

[38] K. L. Johnson, *Contact Mechanics* (Cambridge University Press, Cambridge, 1985).

[39] D. A. Konstantinidis and E. C. Aifantis, Nanostructured Materials **10**, 1111 (1998).

[40] G. M. Pharr and W. C. Oliver, J. Mater. Res. **4**, 94 (1989).

[41] T. A. Michalske and J. E. Houston, Acta mater. **46**, 391 (1998).

[42] N. Agraït, G. Rubio, and S. Vieira, Phys. Rev. Lett. **74**, 3995 (1995).

[43] A. Stalder and U. Dürig, Appl. Phys. Lett. **68**, 637 (1996).

[44] G. Cross, A. Schirmeisen, A. Stalder, P. Grütter, M. Tschudy, and U. Dürig, Phys. Rev. Lett. **80**, 4685 (1998).

[45] A. N. Broers and A. E. Timbs, Microelectron. Eng. **9**, 18 (1989).

[46] A. R. Miedema, Z. Metallkde. **69**, 287 (1978); A. R. Miedema and F. J. A. den Broeder, Z. Metallkde. **70**, 14 (1979).

[47] *Landolt–Börnstein Zahlenwerte und Funktionen aus Physik, Chemie, Astronomie, Geophysik und Technik*, edited by J. Bartels et al., 6th Ed., Vol. II, Part 6 (Springer, Berlin Göttingen Heidelberg, 1959), Chapter 27522, p. 949.

[48] T. Hantschel, P. De Wolf, T. Trenkler, R. Stephenson, and W. Vandervorst, in *Materials and Device Characterization in Micromachining*, edited by C. R. Friedrich and Y. Vladimirsky, *SPIE Proceedings*, Vol. 3512, (SPIE, Bellingham, WA, 1998), pp. 92–103.

[49] V. Shevyakov, S. Lemeshko, and V. Roschin, Nanotechnology **9**, 352 (1998).